Annals of Anatomy 217 (2018) 82–96

Contents lists available at ScienceDirect

Annals of Anatomy

journal homepage: www.elsevier.com/locate/aanat

INVITED REVIEW

Advances in cryo-electron tomography for biology and medicine

Roman I. Koning[a,b,*], Abraham J. Koster[a,b], Thomas H. Sharp[a,*]

[a] Department of Cell and Chemical Biology, Leiden University Medical Center, 2300 RC Leiden, The Netherlands
[b] NeCEN, Institute Biology Leiden, Leiden University, 2300 RA Leiden, The Netherlands

ARTICLE INFO

Article history:
Received 4 September 2017
Received in revised form 2 February 2018
Accepted 5 February 2018

Keywords:
Electron microscopy
Cryo-electron tomography
Energy filter
Phase plate
Direct electron detector

ABSTRACT

Cryo-electron tomography (CET) utilizes a combination of specimen cryo-fixation and multi-angle electron microscopy imaging to produce three-dimensional (3D) volume reconstructions of native-state macromolecular and subcellular biological structures with nanometer-scale resolution. In recent years, cryo-electron microscopy (cryoEM) has experienced a dramatic increase in the attainable resolution of 3D reconstructions, resulting from technical improvements of electron microscopes, improved detector sensitivity, the implementation of phase plates, automated data acquisition schemes, and improved image reconstruction software and hardware. These developments also greatly increased the usability and applicability of CET as a diagnostic and research tool, which is now enabling structural biologists to determine the structure of proteins in their native cellular environment to sub-nanometer resolution. These recent technical developments have stimulated us to update on our previous review (Koning, R.I., Koster, A.J., 2009. Cryo-electron tomography in biology and medicine. Ann Anat 191, 427–445) in which we described the fundamentals of CET. In this follow-up, we extend this basic description in order to explain the aforementioned recent advances, and describe related 3D techniques that can be applied to the anatomy of biological systems that are relevant for medicine.

Contents

Abbreviations: 3D, three-dimensional; cryoEM, cryo-electron microscopy; CCD, charged-coupled device; CEMOVIS, cryo-electron microscopy of vitreous sections; CET, cryo-electron tomography; CLEM, correlative light electron microscopy; CMOS, complementary metal oxide semiconductor; CT, computed tomography; CTF, contrast transfer function; DED, direct electron detector; DQE, detector quantum efficiency; FIB, focused ion beam; fLM, fluorescence light microscopy; GFP, green fluorescent protein; HPF, high-pressure freezing; MRI, magnetic resonance imaging; NMR, nuclear magnetic resonance; PET, positron emission tomography; PSF, point-spread function; SBF, solid block face; SEM, scanning electron microscopy; SIRT, simultaneous iterative reconstruction technique; SPA, single particle analysis; SXT, soft X-ray tomography; TEM, transmission electron microscope; VPP, volta phase plate; WBP, weighted back-projection.

* Corresponding authors at: Department of Cell and Chemical Biology, Leiden University Medical Center, 2300 RC Leiden, The Netherlands.
E-mail addresses: R.I.Koning@lumc.nl (R.I. Koning), T.Sharp@lumc.nl (T.H. Sharp).

https://doi.org/10.1016/j.aanat.2018.02.004
0940-9602/

1. Introduction

Anatomy involves imaging at different length scales, ranging from complete organisms, meters in size, down to single cells with dimensions on the order of micrometers, and even nanometer-scale sub-cellular structures. Consequently, many different techniques are required to visualize anatomical processes over this wide range (Fig. 1). Tomography generates three-dimensional reconstructions and is used in diverse areas of science and medicine, forming the basis of computed tomography (CT), magnetic resonance imaging (MRI), and positron emission tomography (PET). Whilst CT, MRI, and PET can image whole organisms and achieve sub-millimeter resolution, cryo-electron tomography (CET, also known as cryo-ET or electron cryo-tomography; ECT) can image the micrometer to sub-nanometer length scales (Fig. 1). In fact, CET is typically used to visualize individual organelles and biomolecules within cells, yielding insights into the molecular and cellular pathology of diseases (Bauerlein et al., 2017) and pathogens (Wan et al., 2017).

The methodology of CET is fundamentally similar to other tomographic techniques; a volume of material (molecule, virus, cell, organism, etc.) is imaged from multiple angles (different orientations), and is then reconstructed computationally to form a 3D volume (Fig. 2). Whereas in MRI, CT and PET the imaging system is rotated fully around the specimen (i.e. the patient), with CET the specimen is rotated up to a limited angular range within the electron microscope (Fig. 2A). The resulting series of tilt-images (Fig. 2B) is computationally back-projected to reconstruct a 3D volume (Fig. 2C).

In all tomographic imaging techniques, the maximum allowable sample size and the attainable resolution are important practical parameters to consider, as these determine the limits of what can be observed. In CET, the field of view is typically in the order of microns. The sample thickness should be less than 500 nm in order to allow electrons to transmit through the sample with limited specimen-damaging effects due to the coulomb-force interactions of the imaging electron beam with the atoms of the sample. Therefore, in practice, whole cells and tissues must be sliced into sufficiently thin sections before imaging, while small biological specimens, such as purified proteins, viruses and bacteria, can be imaged without sectioning.

The resolution of CET is determined by a combination of the electron radiation dose that can be used to image the sample without detectable damage, detector sensitivity, sample thickness, and the quality of the electromagnetic lenses. Firstly, as electron radiation strongly interacts with atoms (Henderson, 1995), and can therefore be highly damaging for cryo-fixed specimens, the imaging dose must be kept as low as possible. Moreover, in CET this allowable electron dose has to be distributed over many angular views from which the 3D tomogram is reconstructed, resulting in individual images with a low signal-to-noise ratio. Therefore, detectors that efficiently detect electrons with low intrinsic noise levels, are paramount to obtain the highest possible single-to-noise ratio and resolution in the tomogram. With increasing sample thickness, electrons are more likely to undergo multiple scattering events adding to noise. Furthermore, the electromagnetic lenses that are used for imaging are imperfect, which results in image aberrations and loss of resolution. These lens imperfections are, to some extent, well known and characterized for transmission electron microscopy, and can therefore be computationally corrected to achieve the maximum possible resolution (Haider et al., 2009).

Recent advances in cryo-electron microscopy (cryoEM) have given rise to a "resolution revolution" (Kuhlbrandt, 2014), which has increased the number of near-atomic resolution structures of proteins and protein assemblies that emerged using single particle cryoEM (Fernandez-Leiro and Scheres, 2016). The advances that enabled this include technical improvements of the electron microscope, improved detector sensitivity, the implementation of phase plates, automated data acquisition schemes, and improved image reconstruction software and hardware, which, taken all together greatly increase the usability and practical applicability of CET as a diagnostic and research tool.

This review follows up on our earlier publication (Koning and Koster, 2009) and focuses on describing the technical advances that have evolved and emerged since. After recapitulating the general details of cryoEM, the recent improvements on CET are described and discussed in the framework of the practical cryoET workflow.

2. Sample preparation

For imaging samples using CET, the first step is to cryogenically fix the specimen by a method referred to as vitrification. Depending on sample thickness there are two vitrification methods (Fig. 3). Samples that are thinner than 10 μm, such as isolated protein complexes, viruses, bacteria or thin cells, may be vitrified directly by plunge freezing into a cryogen (Dubochet et al., 1988). Samples up to a thickness of 200 μm, such as cell pellets or tissue biopsies, require freezing at high pressure (so-called high-pressure freezing; HPF) for vitrification (Vanhecke et al., 2008). After the vitrification step, samples thicker than 500 nm require thinning prior to imaging. Thinning can be performed by cryo-ultramicrotomy (Al-Amoudi et al., 2004b), using a diamond knife to slice the vitreous ice into sections, or a focused ion beam (FIB) of a heavy metal (e.g. gallium) to ablate the material to a specified thickness.

2.1. Vitrification of thin samples

In order to be suitable for CET, biological samples need to be preserved in vitrified ice, an amorphous state of ice that closely resembles that of liquid water (Dubochet et al., 1988). Vitrification can be obtained by cooling the water faster than the rate of water crystallization. At high cooling rates ($\sim 10^5$ K/s), thin biological samples (<~10 μm thick) with high water content are effectively fixed in vitreous ice at cryogenic temperatures (100 K) (Dubochet et al., 1988). For samples thicker than 10 μm, the rate of heat extraction becomes limited by the heat capacity of water in the sample, resulting in slower cooling rates and formation of crystalline ice (Studer et al., 2008).

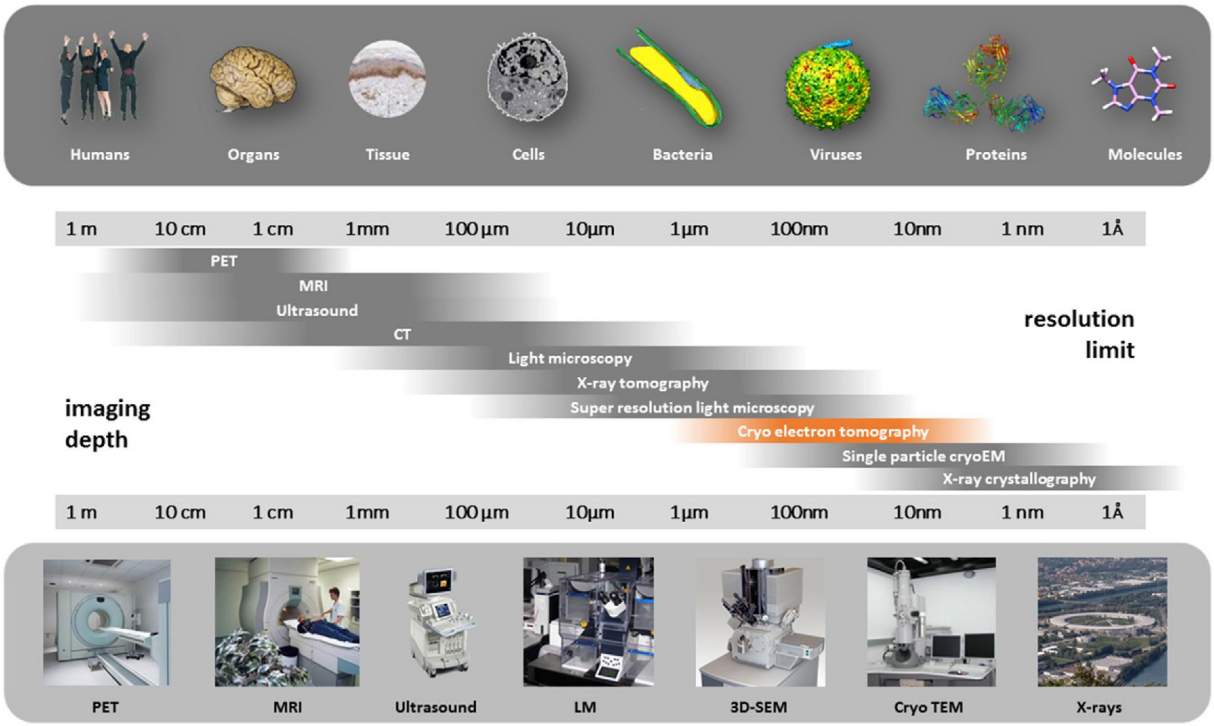

Fig. 1. Scales and resolution of medical imaging techniques.
Specimens of different length scales require diverse imaging techniques with particular limits in imaging depths and resolutions.

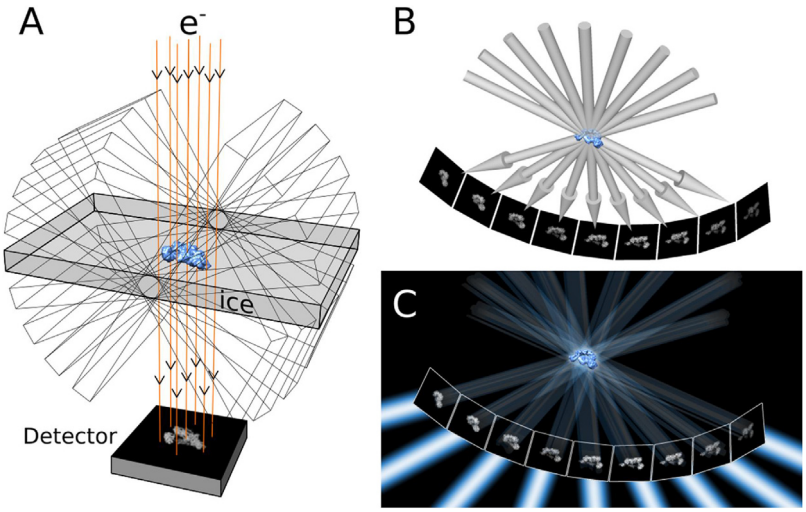

Fig. 2. Cryo-electron tomography methodology.
(A) In the transmission electron microscope, a series of images is acquired on a detector from a sample of interest, as the sample is rotated to specified angles. The sample is embedded in vitreous ice and can be very diverse, e.g. whole cells, cellular extracts, proteins or other biomolecules. (B) The resulting projection images of the specimen from different angular views yields a so-called tilt-series. (C) This tilt-series is computationally back-projected to form a 3D volume, the tomogram.

The most straightforward way to vitrify is to use instrumentation developed for plunge-freezing. These devices allow control over cryogen temperature, as well as parameters such as blot time, humidity and temperature in the vicinity of the grid before and during plunging, which improves reproducibility and enables freezing of live cells cultured on grids. Thin samples are vitrified by directly plunging them into a cryogen with high heat capacity and thermal conductivity, such as liquid ethane at its melting temperature of ~90 K. Practically, for purified protein samples, typically 2–5 µl is applied on the grid and, in order to make the sample sufficiently thin for vitrification, most fluid is removed by blotting with filter paper to leave a thin layer of liquid (typically 30–100 nm) over the carbon-film support. In order to form and maintain a thin, stable layer of liquid, the carbon support is rendered in a hydrophilic manner by glow-discharging or plasma-cleaning prior to the application of the sample, which facilitates liquid spreading over the support film. Typically, holey-carbon or lacey-carbon films are used as a sample support film. Holey-carbon films consist of regularly spaced holes with a specified diameter (typically 1–2 µm) and are commonly used for automated data collection for single-particle analysis. Alternatively, lacey-carbon films comprise randomly sized and closely-spaced holes with variable diameter that allows a distribution of ice-thicknesses, which can be desirable for isomorphic structures that are present in a variety of sizes, such as cell lysates of

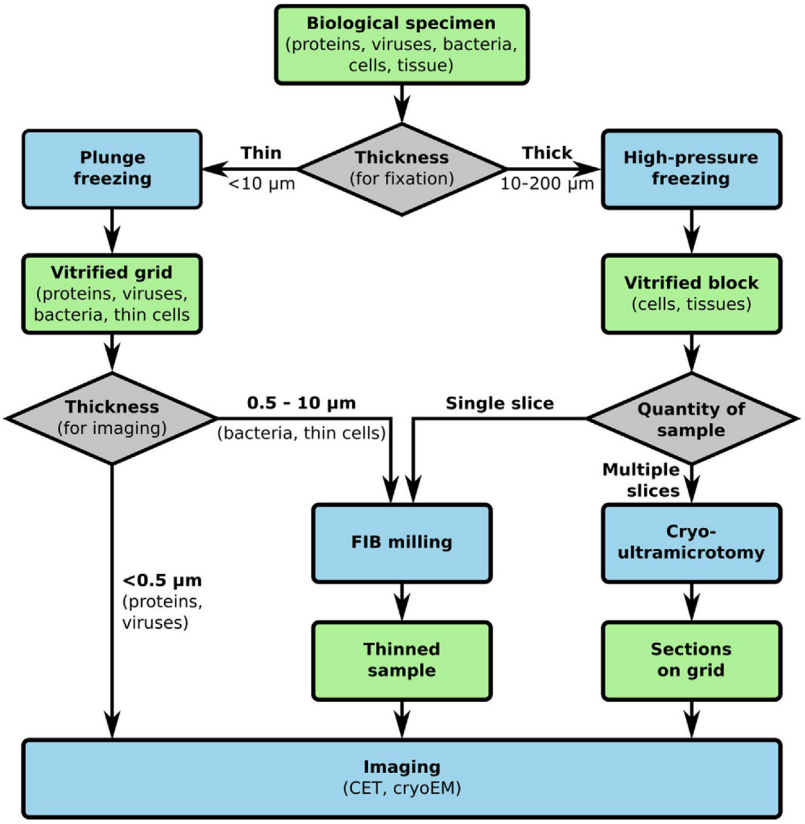

Fig. 3. Cryo electron microscopy sample preparation flow chart.
Sample preparation flowchart for cryoEM in which choices (grey) for several preparation and visualization techniques (blue) depend on: (i) the sample thickness, and (ii) the desired structures to be visualized. Samples (green) thinner than 10 µm (e.g. proteins, viruses, bacteria) can be vitrified by plunge-freezing, while thicker samples (e.g. cell pellets or tissue blocks/biopsies) can be cryo-fixed by HPF. Samples thicker than ~500 nm (e.g. cells and tissue) must be thinned prior to imaging in order to ensure electron transparency. Thinning can be performed either by cryo-ultramicrotomy or cryo-FIB-milling. Finally, cryo-preserved samples thinner than 500 nm can be imaged by 2D cryoEM (projection imaging or single particle analysis) or 3D CET (tilt series acquisition for tomography or sub-tomogram averaging). (For interpretation of the references to color in this figure legend, the reader is referred to the web version of this article.)

liposomes. For cryoEM of cellular samples that are cultured directly on the grid, gold grids are used as a substrate to avoid the cytotoxicity of copper.

2.2. High pressure freezing for thick samples and whole cells

High-pressure freezing (HPF) can be used to vitrify samples up to 200 µm in thickness (Dahl and Staehelin, 1989; McDonald and Auer, 2006; Moor and Riehle, 1968), and is essential for cryo-fixation of adherent cells, cell pellets, tissues and biopsies. With HPF, high pressure is applied to a sample during freezing, the expansion of water during crystallization is counteracted (le Chatalier's principle), inhibiting the formation of hexagonal ice crystals (the common form of ice found in freezers) and thereby promoting the formation of vitrified ice.

Dedicated HPF apparatuses (Studer et al., 2001) freeze samples within ~20 ms at 200 MPa using a jet of liquid nitrogen at 77 K (−196 °C) in a controlled and reproducible way. With the addition of a rapid transfer system (Verkade, 2008), correlative light electron microscopy imaging (CLEM, see below) is facilitated by making it practically possible to vitrify the sample within ~4 s after imaging with (fluorescent) light microscopy.

A recently proposed, relatively straightforward method for HPF utilizes self-pressurization, in which the sample is contained within a closed copper capillary tube (Leunissen and Yi, 2009). Upon cooling the tube in liquid nitrogen, the closed tube freezes from the outside, which increases the pressure in the center. This method excludes the need for specialist HPF equipment, although the use of cryo-protectants within the samples appears to be necessary to maximize the success-rate of high-quality sample preservation (Han et al., 2012).

2.3. Cryo-sectioning thick samples

Specimens thicker than 500 nm, prepared by either plunge-freezing or HPF, require thinning prior to imaging with CET. This thinning must be performed below ~140 K (~−130 °C), the temperature above which vitreous ice begins to recrystallize (known as devitrification). Thinning can be performed using a diamond knife to slice the sample into many thin sections (e.g. 50–150 nm) using ultramicrotomy at cryogenic temperature, often referred to as cryo-sectioning or cryo-electron microscopy of vitreous sections (CEMOVIS) (Al-Amoudi et al., 2004a). CEMOVIS combines cryo-preservation with the possibility to image slices from thick samples, and enables high resolution imaging of e.g. vitrified cells that could not be visualized otherwise (Al-Amoudi et al., 2004b). Cryo-sectioning of vitreous samples is technically demanding and can introduce artifacts which distort the sample, such as blade marks and compression fractures (Richter, 1994). Many of these cryo-sections can be transferred onto an EM grid, and multiple sections can be imaged by CET.

Alternatively, focused ion-beam (FIB) milling can be used to remove unwanted material surrounding the region of interest by ablation using a beam of heavy-metal ions (e.g. gallium). FIB milling was originally developed for material sciences to prepare e.g. thin slices of semiconductors and other inorganic materials (Krueger,

1999). Recently, dedicated scanning electron microscopes have been developed to facilitate FIB milling of vitrified biological material prepared by both HPF (Hayles et al., 2010) and plunge-freezing (Marko et al., 2007) samples which cannot be thinned by cryo-sectioning (Fig. 3). While FIB milling results in a single cellular slice, cryo-sectioning can be used to image multiple, sequential sections. Gallium ions are expected to deposit on milled surfaces and in the sections, and irregularities of the milled surface often occur, which in extreme cases can lead to problems during imaging (Rigort et al., 2012a; Rigort and Plitzko, 2015).

2.4. Stability of vitreous samples in the electron microscope

After cryo-fixation, during storage, transport, thinning, transfer into the TEM and image acquisition, the temperature of the sample must be maintained below ~140 K (~−130 °C) to avoid devitrification. In addition, samples must be kept free from contamination, such as the adhesion of small ice-crystals that may float in liquid nitrogen, at all times. Therefore, cryoEM grids are typically kept and transferred in closed storage boxes under nitrogen liquid or gas at ~77 K (−196 °C) before being inserted into the TEM.

Most electron microscopes are used for both conventional (room temperature) EM and cryoEM. They use a removable cryo-holder when performing cryoEM, which is inserted into the side of the TEM column (a so-called side-entry system). The cryo-holder comprises a Dewar filled with liquid nitrogen to maintain the grid at 95 K (−178 °C). The Dewar must be refilled manually with liquid nitrogen every few hours, which limits the ability to automate data collection for a prolonged period of time. The mechanical stability of the sample is also limited by the temperature instability of the cryo-holder caused by diminishing liquid nitrogen levels and heat flow between the holder and the microscope. This causes the sample to drift over time, further limiting the ability to automate data collection over the course of hours.

When working with a side-entry system, EM grids are loaded individually, and therefore each new sample requires re-insertion of the cryo-holder into the TEM. Each insertion deteriorates the low-pressure environment within the TEM-column near the sample, and subsequently increases the chance of contamination of the EM grid. Moreover, over time the sample thickness can increase due to ice growth on the sample within the TEM column, limiting the measuring time that can be used to collect a tilt series.

During the last five years, many of these limitations have been removed with the development and introduction of novel types of electron microscopes dedicated to perform cryoEM for a prolonged time-period. These types of TEM have an automated specimen loading system that holds multiple grids and automatically transfers them into a continuously cryogenically-cooled and stable specimen stage without disrupting the high vacuum environment. Additionally, the quality of the vacuum system of these type of TEMs is significantly enhanced, which results in negligible ice growth on the sample over the course of days, allowing extended automated data collection.

3. Data collection

3.1. Tilt series acquisition

Electrons damage biological specimens (Glaeser, 1971) and as such the electron dose exposed to the sample must be minimized. This can be achieved using a search, focus and image scheme (a so-called low-dose scheme) during data collection, whereby the desired imaging locations are identified at low magnification (and hence low electron dose) while focusing is performed at a location adjacent to the area of interest prior to image acquisition. This minimizes the amount of dose, and hence damage that the area of interest is exposed to and maximizes the achievable resolution. The total dose used for imaging must still be very low, typically less than 100 $e^-/Å^2$, to achieve nanometer resolution (Fig. 3, top row). Because tomography is based on imaging the same region from multiple angles, this dose has to be distributed (fractionated) over the number of images that is used to record a tilt image. Tilt series are typically collected from ±60°, with a separation of 2° between images; each tilt series therefore images the same location ~61 times, resulting in a dose of less than 2 $e^-/Å^2$ for each tilt image. During tilting, the apparent thickness of the sample increases as $1/\cos(\theta)$, where θ is the tilt angle. Samples appear 2× thicker at 60° tilt, hence the distance that electrons must transmit through, and the likelihood of multiple scattering events with the atoms within the sample, also increases. Consequently, the fractionated electron dose of the tilt series results in low contrast and high levels of noise in the individual images (Fig. 3, bottom row, left image), which makes accurate alignment of a tilt series challenging. To facilitate and improve the accuracy of alignment, gold fiducial markers between 5–25 nm in diameter are generally added to the sample (or on the specimen support) immediately prior to vitrification. These fiducial markers have high contrast in the low-dose images, and can be computationally tracked as point-like objects to align the images prior to 3D reconstruction (Luther et al., 1988; Walz et al., 1997).

Overall, the resulting low dose that has to be used for imaging to minimize radiation-induced specimen damage results in noisy images in the tilt series (Fig. 4), which hampers accurate alignment of a tilt series. As a consequence, cryo-electron tomograms will typically exhibit high noise levels, low contrast and limited resolution. Technical improvements that increase the signal-to-noise ratio in the individual images of a tilt series have a direct effect on improving the quality of the resulting cryo-tomograms. During the last three years, the quality of data collected for cryo-tomography has improved significantly, primarily by three major developments: phase plates, energy filters and direct electron detectors.

3.2. Phase plates improve tomogram interpretability

As cryoEM samples are very thin (less than a few hundred nanometers) and are composed of relatively light elements (typically carbon, hydrogen, oxygen and nitrogen), the contrast forming mechanism can be very well described by (weak−) phase contrast imaging. Phase contrast is generated by phase differences that occur between an unscattered electron wave (the majority of the electrons that do not interact with the sample) and the electron waves that interact with atoms within the sample. To transpose this phase shift into a measurable contrast, images are typically taken out of focus, which increases low-resolution image contrast but negatively affects the high resolution in the images. The way that the phase (and amplitude) of the electron waves are influenced by the objective lens of the microscope (e.g. defocusing) can be mathematically described by the contrast transfer function (CTF) (Marabini et al., 2015). The CTF describes an inverse relationship between contrast and resolution, and additionally predicts contrast reversals at certain frequencies, resulting in fringes in EM images. Fortunately, images can be (partly) corrected for the CTF, which relies on accurate defocus determination. CTF correction in CET is not always a trivial task since images are tilted and focus varies within individual images. Nonetheless, CTF correction can also increase the resolution of tomograms (Fernandez et al., 2006; Turonova et al., 2017; Xiong et al., 2009).

One of the most exciting developments for CET is the advent of reliable and commercially available phase plates. Phase plates increase image contrast at low resolution and remove the need for defocusing, resulting in higher resolution images without CTF

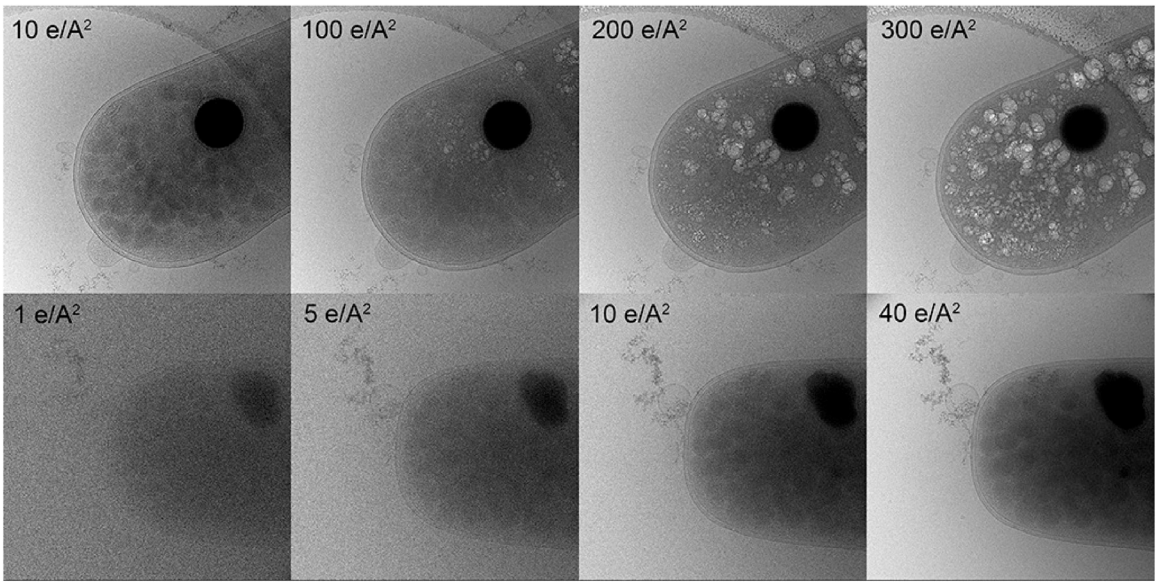

Fig. 4. Radiation damage and electron dose.
Electron radiation damage of cryo-samples of (gammaproteo) bacteria occurs directly upon imaging and increases with dose. High-resolution atomic features are lost within a few electrons per Å² (e/Å²) while visible damage occurs later (top row, total electron dose). Because of radiation damage the electron dose for imaging is limited, which greatly affects the signal-to-noise ratio in typical cryoEM images (bottom row, electron dose per image).

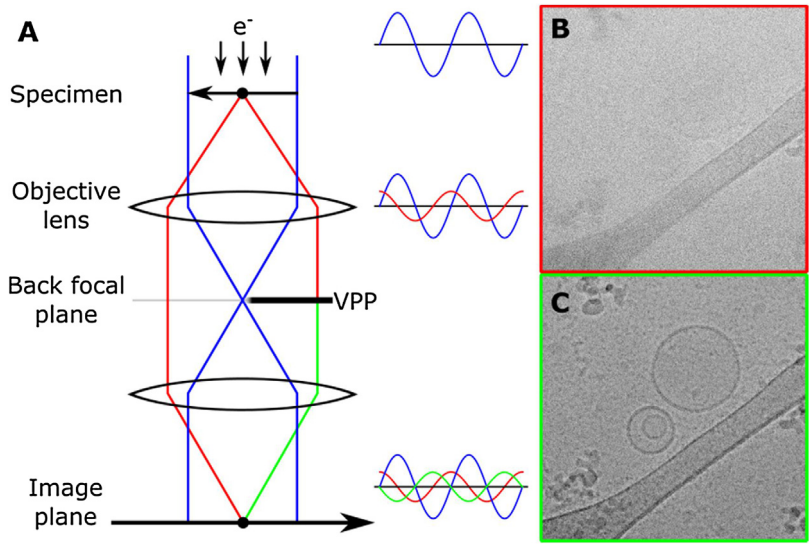

Fig. 5. The Volta phase plate increases the contrast of electron tomograms.
(A) Incoming electron waves (blue) have a certain phase and amplitude. Transmitted, non-diffracted, electrons (blue) do not interact with the specimen and their phase is unaffected. In contrast, some of the electron wave is diffracted by the specimen (red), which retards the phase of the diffracted wave by quarter of a wavelength. This small phase shift causes only minimal contrast of the magnified specimen (B). In the presence of the VPP the diffracted wave is retarded further, ideally by another quarter of a wavelength (green), placing it 180° out of phase with the non-diffracted transmitted wave (blue), resulting in maximal negative phase contrast (C). Micrographs acquired at focus of vitrified liposomes and lacey-carbon film in the absence (B) and presence (C) of the VPP, demonstrating the contrast improvement.

correction, compared to images acquired using defocus contrast. Electrons are diffracted by interaction with thin biological specimens, which behave as weak phase objects and retard the phase of the diffracted electron wave with respect to the transmitted (non-diffracted) electron wave by a quarter of a wavelength (Fig. 5A), but not the amplitude, so that very little contrast is visible at low frequency (Fig. 5B). Unfortunately, the phase information is lost and only amplitude data is collected by the detector in the form of intensity. So-called Zernike-type phase plates further shift the diffracted electron waves, generating an approximate half-wavelength phase shift with respect to the non-diffracted electrons, turning this phase information into measurable amplitude contrast without the need to defocus (Fig. 5C) (Danev and Nagayama, 2001). This results in destructive interference and maximal contrast at low resolution (Fig. 5C), which makes projection images and reconstructed tomograms much more readily interpretable (Fukuda et al., 2015; Sharp et al., 2016).

Phase plates for EM were previously described, but their practical use was limited due to charging and short lifetimes (Dai et al., 2013; Danev et al., 2009; Danev and Nagayama, 2001). In 2014, Danev et al. developed the Volta phase plate (VPP) (Danev et al., 2014), which uses a beam-induced method (Malac et al., 2012) to generate the additional phase shift (Fig. 5) on top of the phase shift of the diffracted electrons, induced by the specimen. The central non-diffracted electrons create a local Volta (electrostatic) potential (hence the name VPP) in the amorphous carbon of the

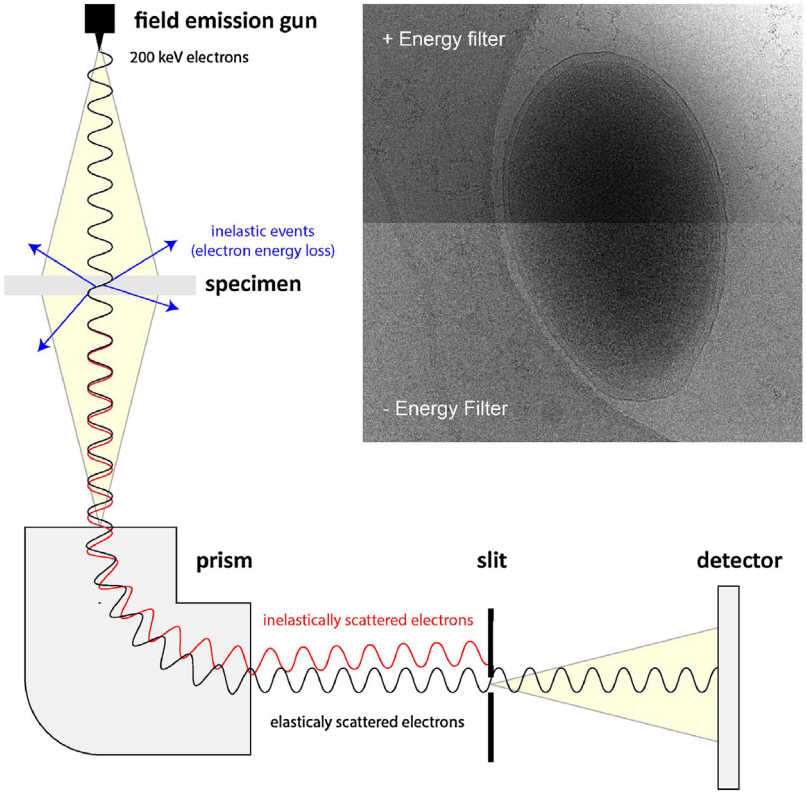

Fig. 6. Energy filtering.
Electrons with a certain energy (here 200 keV ± 1 eV) are emitted from an electron source (FEG). Elastic interactions with the specimen do not result in energy loss (black wave) while inelastic interactions lead to lower energy electrons that have a longer wavelength (red wave). A prism lens transfers this difference into a shift of the electrons that have lost energy, which are removed by a slit. Inset shows that an energy filtered image is less bright but has more contrast than an unfiltered image. (For interpretation of the references to color in this figure legend, the reader is referred to the web version of this article.)

phase plate. The transmitted electrons pass through this local Volta potential without their phase being affected, whilst the diffracted electrons interact with the rest of the phase plate and are retarded by a further quarter-wavelength by interaction with the carbon of specific thickness, thereby generating a half-wave phase shift with respect to the transmitted electrons (Fig. 5). Because the transmitted electron beam creates the local phase shift, the VPP requires minimal physical alignment, and the Volta potential can be generated on the carbon film when and where desired, facilitating automated data collection. However, since the phase shift is generated by irradiation with electrons (known as conditioning) the amount is dependent on the electron dose, which results in unstable phase shifts (Danev et al., 2014; Sharp et al., 2017). Nevertheless, the variable phase shifts still increase the contrast of the tomogram, and the VPP has already shown potential for in situ structure determination of complement activation (Sharp et al., 2017) and membrane attack complex pore formation (Sharp et al., 2016) on liposomes, as well as the cellular distribution of proteasomes, ribosomes and nuclear pore complexes (Asano et al., 2015; Mahamid et al., 2016).

3.3. *Energy-filtering reduces noise*

When electrons are incident on a sample they can interact with the sample in either an elastic event, where no energy is transferred between electron and specimen, an inelastic event, where energy is lost to the specimen, or the electrons do not interact with the sample and are transmitted unaffected (Egerton, 2011). Inelastically scattered electrons contribute to the noise within the image and damage the specimen by breaking molecular bonds, localized heating, and evolution of hydrogen gas, among other effects (Baker and Rubinstein, 2010). The ratio of scattered versus unscattered electrons can be predicted based on the mean free path of these electrons, the average distance travelled between two successive scattering events. This mean free path for 200–300 keV electrons is on the order of 200–300 nm (Feja and Aebi, 1999; Grimm et al., 1996) and is different for elastic and inelastic events. The likelihood of these events therefore shifts depending on sample thickness. In cryoEM samples that are less than 100 nm thick, most electrons pass through the sample unscattered, while the rest mainly scatter only once, either elastically or inelastically. However, the likelihood that electrons scatter more than once increases quickly with specimen thickness (Han et al., 1995). Since multiple scattered electrons result in noise in the image, samples are preferably not thicker than the mean free path. With samples that have a thickness of one to two times the mean free path, such as bacterial cells and thin adherent cells, removal of the inelastically scattered electrons can significantly increase image contrast. This can be achieved by using an energy filter to block electrons that have lost or gained energy.

Energy filters separate the electrons based on their wavelength (Fig. 6) in a way that is comparable to a prism for photons. Energy filters contain one or more prism lenses that bend the electron wave, after which it gets spatially separated, depending on the electron energy. The incoming electrons must therefore have a very low energy spread, and for this reason energy filters are often used in combination with Field Emission Guns (FEGs), which produce electrons with an energy spread in the order of only a few eV. By putting a physical slit in the path of the beam in combination with varying the energy of the primary electron beam, electrons with a specific energy can be transmitted and detected (Krivanek et al., 1995; Lanio et al., 1986; Tanaka et al., 1999). Energy filters that transmit only electrons with the same energy as the incident pri-

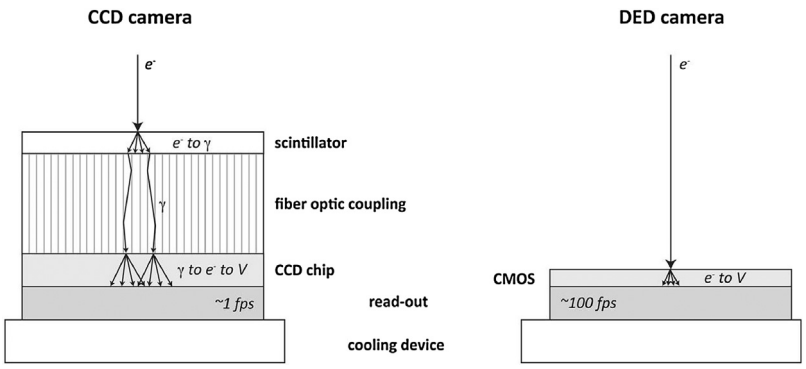

Fig. 7. Electron detectors.
(A) Typical layouts of CCD (charge coupled device) camera and CMOS (complementary metal oxide semiconductor) direct electron detector (DED). CCD cameras detect electrons (e^-) via a luminescent scintillator layer that converts electrons into light (γ). This light is transferred via a fiber optic coupling into a CCD chip, which converts the light into a voltage on a square array of pixels that is read out in a few seconds, resulting in a digital image. (B) In contrast, a direct electron detector CMOS chip directly detects incoming electrons and converts them into a voltage over an array of pixels that can be read out at high speed.

mary electron beam operate in a so-called zero-loss imaging mode, removing the background noise due to inelastically scattered electrons. Consequently, the contrast of the resultant image is increased by ~16% compared to unfiltered images (Fukuda et al., 2015). Apart from being useful for thicker specimens, it is also useful in tomography, where, upon tilting, the slab-shaped specimen effectively gets thicker at high tilt angles. Zero-loss energy filtering can be used together with phase plate imaging, and provide an ~68% increase in contrast when used in combination (Fukuda et al., 2015).

3.4. Direct electron detectors

Electron micrographs were originally acquired on photographic film, which needs to be developed and scanned before data analysis or tomogram reconstruction. Digital cameras are much more convenient due to their near-instantaneous readout. The first digital detectors for EM were charged-couple device (CCD) cameras (Dierksen et al., 1995; Koster et al., 1992; Krivanek and Mooney, 1993; Spence and Zuo, 1988) (Fig. 7A). CCD cameras incorporate a luminescent scintillator layer that converts incident electrons to photons, and the scintillator layer is connected to a CCD chip by fiber-coupled optics (Fig. 7A), which spreads the electron signal over a large area depending on the thickness of the scintillator, resulting in lower resolution images. This spreading of the signal can be described by a so-called point-spread function (PSF). Another important effect of this design is that not all incoming electrons are registered as photons on the chip. The likelihood that an incident electron is actually registered is described by the detector quantum efficiency (DQE). Ideally, all electrons are detected and no signal coming from the sample is lost. Furthermore, it is important that digital cameras have a high dynamic range, can detect both low and high levels of electrons, and their response over this brightness range is linear. So, overall, good detectors can be defined by having a small PSF, a high DQE and ideally a linear sensitivity over a high dynamic range.

The primary reason for the resolution revolution impacting EM is the advent of direct electron detectors (DEDs) (Xuong et al., 2007). DEDs directly convert electrons into an electrical signal for output detection (Fig. 6B). They very efficiently detect electrons, which results in a high DQE, much better than film (McMullan et al., 2014). Therefore, also the PSF now depends on scattering of electrons inside the detector itself, which can be minimized by making the detector as thin as possible. Another advantage of DEDs is their fast readout, which can reach a few hundred frames per second. Instead of single images, movies of the sample can be recorded. This is useful since irradiation by the electron beam and the resulting beam damage of the sample can result in image movement and unpredictable local distortions within the sample itself. By recording movies, these movements and distortions can be corrected by a posteriori alignment and distortion-correction of the frames, which compensates for sample movement and increases the resolution of the image. Another advantage of the fast readout is seen when a low electron dose is used and thus individual electrons can be detected. In fact, single electrons can be localized with sub-pixel accuracy, so-called super-resolution mode, which also positively affects the DQE of the camera (McMullan et al., 2014). In SPA, now near atomic resolution maps are regularly produced of protein and protein complexes (Merk et al., 2016). In tomography, the resolution increase resulting from DEDs has enabled visualization of proteins inside cells and also near-atomic resolution maps using sub-tomogram averaging (Schur et al., 2016).

3.5. Automated data collection and storage

Tomographic data can be acquired automatically by several programs, of which serialEM (Mastronarde, 2005), UCSF tomography (Zheng et al., 2004), TOM (Nickell et al., 2005), and Xplore3D/Tomo4 (Thermo-Fischer, formerly FEI company) are most commonly used. Although these are developed from different perspectives (e.g. type of sample, type of microscope, type of users), these programs in essence perform the same routines (Koster et al., 1992; Ziese et al., 2002). With the current improvements in hardware, tomographic acquisition software is targeted towards automated recording of multiple tilt-series over several days, with the support of movie-mode recording by direct electron detector cameras and the Volta phase plate.

Automated data collection and movie-mode super-resolution imaging has far-reaching consequences for image processing and data storage. The number of datasets that can be recorded per day increases one factor, while the size of a single tomogram tilt series dataset, typically ~1 Gb can effectively increase between one or two factors, with a 4× increase going from normal to super-resolution mode and typically 7–30× increase due to the frames used in movie recording. These large datasets need CTF correction, movie alignment and tomographic image processing. Standard desktop computers hardly suffice, and workstations are often employed for computation.

Deposition of raw data in online, publically-accessible databases is increasingly important for structure validation, method development and training (Iudin et al., 2016). Additionally, deposition of tomographic reconstructions and surface rendering data (see Section 4.4 below) enables integration of CET data with protein

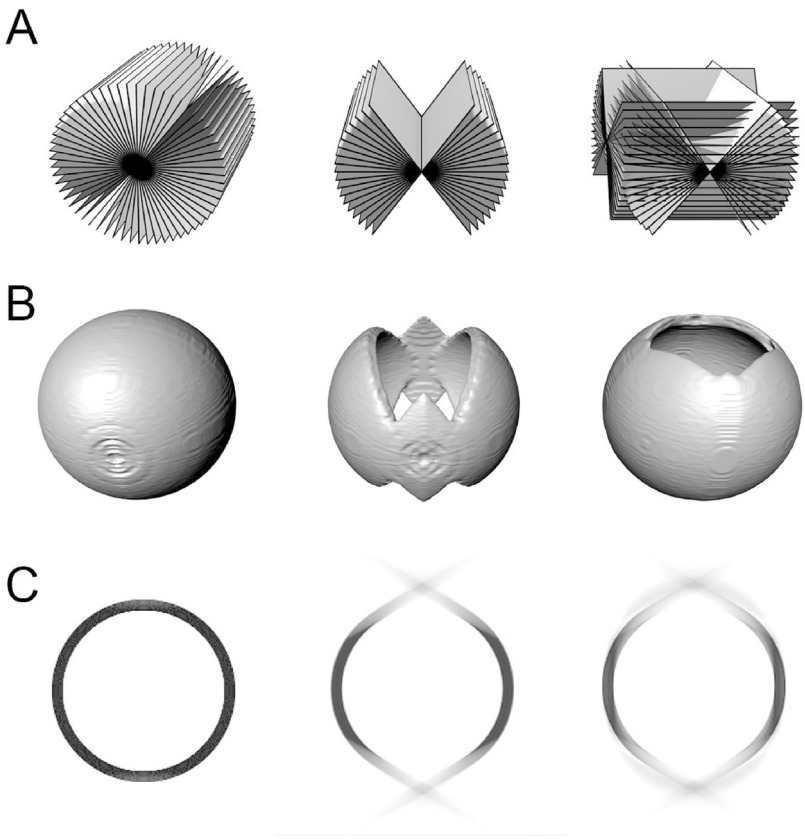

Fig. 8. Layout of single and dual axis tilt series in Fourier space.
Effect of angular sampling and missing wedge on the resolution in tomograms. The effect of the angular sampling and the missing wedge in tomography shown in Fourier space slices (a), surface renderings of a reconstructed thin-shelled sphere (b), and YZ slices through the corresponding tomogram (c). The left column shows the situation when there is full angular sampling along one tilt axis (the X-axis).
The top image shows that Fourier space is sampled equally in the YZ plane. The surface rendering and a central slice of the tomogram indicate no anisotropic resolution in the reconstructed sphere in those directions. The middle column shows the situation when there is limited tilt angle (from −60° to +60°) along a single axis. The result will be a missing wedge in Fourier space that can be observed in the surface rendering and as diminishing density at the top and bottom of a reconstructed sphere (b) and an elongation in the YZ slice. The right column shows the situation when two tomograms are combined from two orthogonal tilt axes (dual-axis tomography) with limited rotation between −60° and +60°. In Fourier space, the missing wedge is reduced to a missing pyramid, and the anisotropy in the resolution along the Y-axis is reduced (from G. van Tendeloo, D. van Dyck and S.J. Pennycook "Handbook of Nanoscopy", chapter 36, page 1313. 2012. Copyright Wiley-VCH Verlag GmbH & Co. KGaA. Reproduced with permission).

structure databases, such as the protein database (PDB) (Bernstein et al., 1977) and other imaging modalities (Patwardhan et al., 2014; Patwardhan et al., 2017).

4. Image processing

4.1. Tomogram reconstruction automation

Typically, reconstruction of cryo-electron tomograms consists of four steps; pre-processing, tilt-series alignment, post-processing, and reconstruction. Preprocessing involves truncation of extreme data values caused by X-rays or occlusion by the EM grid. Tilt-series alignment is necessary as the sample is not rotated perfectly during acquisition. Obvious whole-image movements caused by imperfect stage bearings can be aligned using cross-correlation of the images. Smaller and local distortions are caused by beam induced movement, specimen drift and defocus effects. For low-contrast CET tilt series, fine alignment is usually performed by tracking high-contrast fiducial markers, 5–25 nm gold beads that are added to the sample prior to vitrification specifically to aid alignment (Luther et al., 1988; Walz et al., 1997). However, alternative methods, such as cross-correlation and patch tracking, are available that do not require the addition of fiducials to the sample (Amat et al., 2010; Guckenberger, 1982). Accurate fine alignment is critical, as poor alignment results in projection mismatch and limits the resolution of the resulting tomogram. Micrograph post-processing includes CTF correction and noise filtering. Finally, 3D reconstructions can be achieved by either Fourier-space algorithms, such as weighted back-projection (WBP) (Radermacher, 1988), or real-space methods, such as simultaneous iterative reconstruction technique (SIRT) (Gilbert, 1972). WBP is more common, and involves taking a Fourier transform of each image before placing these slices into a 3D Fourier volume at the angles specified during tilt series acquisition. The Fourier components of each slice are then weighted depending on their frequency to prevent oversampling of low-resolution details. Next, an inverse Fourier transform back-projects the volume into real-space, yielding a tomographic volume. Reconstruction using WBP is generally faster than SIRT, although WBP tomograms can be dominated by high-frequency noise, whereas real-space reconstruction methods, such as SIRT, generally take longer due to the iterative nature of the method, although noise is suppressed.

With the automation of data collection, the number of tilt series produced per day increases, resulting in terabytes of data and several tens of tilt series being collected each day. Rough tilt series alignment and initial tomogram generation are easily performed but since samples and tilt series are quite different in composition and quality, reconstructions need individual attention and

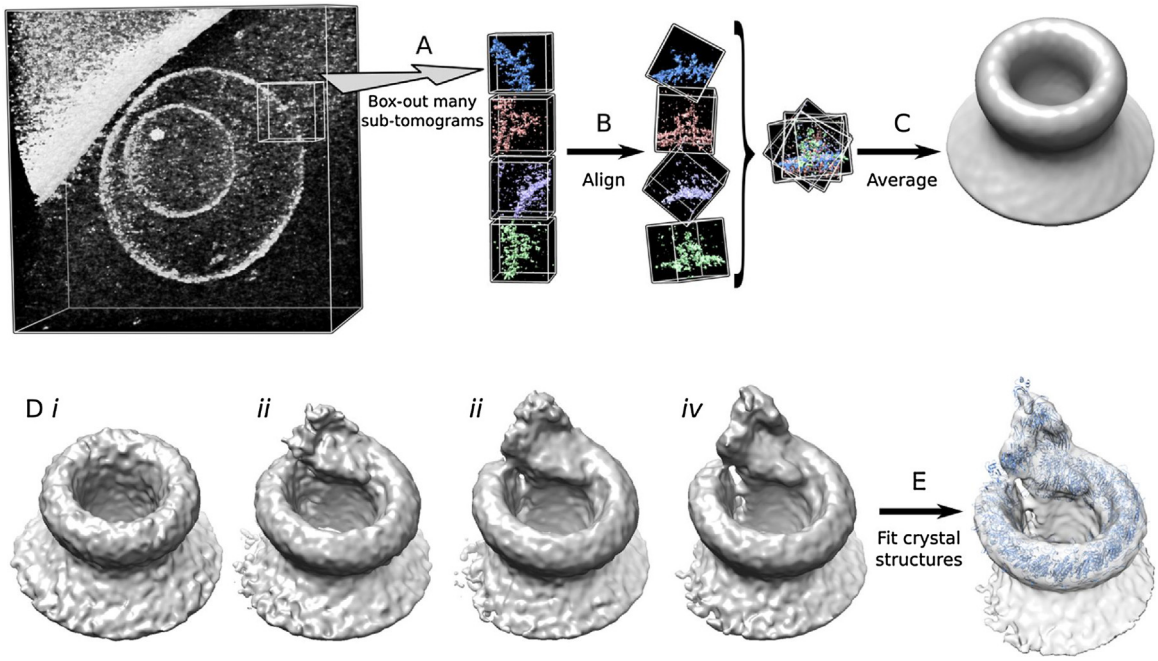

Fig. 9. Sub-tomogram averaging.
(A) From a tomographic volume, sub-volumes containing single particles of the same biological structure are extracted from tomographic volumes. In this case, the particle is a membrane attack complex (MAC) pore perforating a liposome. The particles are aligned (B) and averaged (C) to generate an initial map. (D) Particles are then iteratively re-aligned to the previous map and averaged to generate improved maps (i–iv). (E) The final map with the highest resolution is achieved when an iteration does not generate any improvement, and can be interpreted with the use of crystal structures (EMD-3289 (Sharp et al., 2016)).

manual processing to achieve the best quality. Reconstructing tomograms from a tilt series was originally an interactive, labor-intensive process in which many steps were manually performed and checked, especially gold fiducial fine alignment, in order to generate a high-quality tomogram. Since manual tomogram reconstruction is rather inefficient and slower than data acquisition time, automated tilt series image alignment and tomogram reconstruction procedures are highly desirable. Recently, several automated fiducial marked based and marker-free fine alignment schemes have been developed (Castano-Diez et al., 2010; Han et al., 2015; Sorzano et al., 2009) and implemented in several packages such as IMOD (Mastronarde and Held, 2017), Protomo (Noble and Stagg, 2015) and UCSF tomo (Zheng et al., 2011) (for an extensive list of tomography packages see https://en.wikibooks.org/wiki/Software_Tools_For_Molecular_Microscopy), as well as in dual axis tilt series (Winkler and Taylor, 2013). Furthermore, several packages with additional database storage are available (Ding et al., 2015; Zheng et al., 2007).

4.2. The missing wedge limits interpretation of tomographic volumes

Due to the geometry of both the specimen/EM grid and objective lens of the microscope, tilt series are typically collected over an angular range between ±60° (Fig. 1). This results in a "missing wedge" of data (in Fourier space), causing anisotropic resolution in the tomogram, which is seen as loss of resolution in the axial direction (Fig. 8) (Diebolder et al., 2015; Sharp et al., 2017). Anisotropic resolution is also influenced by the missing information between sequential tilt images, which have angular steps of 2–3° (Koster et al., 1997). Anisotropy can be reduced using dual-axis tomography, whereby two tilt series are acquired with a relative 90° in plane rotation (Penczek et al., 1995). The two resulting tomograms are then aligned and combined into a single tomographic volume. This procedure reduces the missing wedge into a "missing pyramid", which eliminates anisotropy especially in the plane orthogonal to the tilt axis (Mastronarde, 1997), but does not remove blurring of the reconstruction along the direction of the electron beam. Dual-tilt tomography requires that the same region is imaged twice and therefore it is necessary to fractionate the electron dose over both tilt series in order to prevent increased radiation damage. Therefore, each of both dual axis tilt series receives half of the total dose compared to a single series and thus these either have very poor-contrast images or half the number of images.

One method to eliminate the missing data entirely is imaging a rod-shaped sample in a holder that can be rotated by a full 180° (Palmer and Lowe, 2014). Alternatively, in case the tomogram contains many identical copies of a protein complex or particle, the missing data of these particles can be filled in by volume averaging, known as sub-tomogram averaging.

4.3. Sub-tomogram averaging and template matching

Electron tomograms are by no means ideal reconstructions of the sample. The resolution is limited by electron beam-induced specimen damage and the poor signal-to-noise ratio in the acquired tilt series. Furthermore, the limited tilt range results in incomplete sampling, causing anisotropy of the reconstruction. While for complete tomograms this is difficult to overcome, in cases where the reconstructed volume contains multiple identical structures, both the isotropy and the resolution of these can be recovered by averaging multiple sub-volumes from the tomogram. This process is known as sub-tomogram averaging or single-particle tomography (Fig. 9). This chimera between CET and single-particle analysis is especially utilized to determine macromolecular structures (Grange et al., 2017) and their structural variety (Unverdorben et al., 2014) in native biological environments and membrane bound structures (Pfeffer et al., 2012; Sharp et al., 2016). Generally, the electron dose used during tomographic tilt series which is used for sub-tomogram averaging is minimized to limit beam damage. The resulting loss of signal is then recovered by averaging identical sub-tomograms. When using specialized tilt schemes and meth-

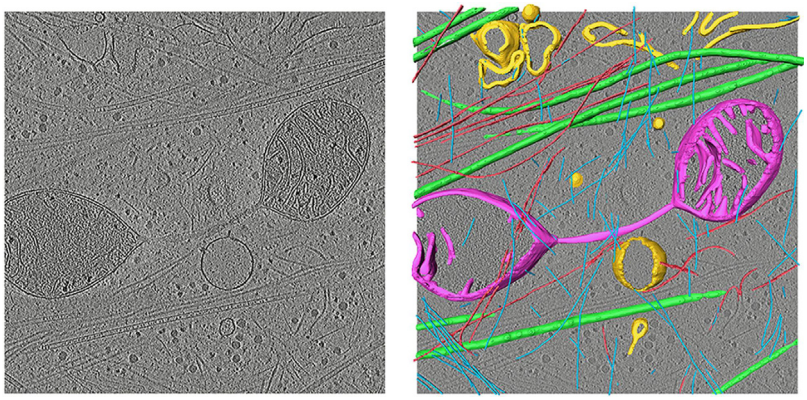

Fig. 10. Surface rendering of cellular cryo electron tomograms.
(A) A slice through a cryo-electron tomogram of a cell shows all kinds of structures in 2D. (B) Some structural densities can be surface rendered by template matching, e.g. actin (blue), while others are drawn in by hand: lipid membranes (yellow), microtubules (green), mitochondria (purple), and intermediate filaments (red). (For interpretation of the references to color in this figure legend, the reader is referred to the web version of this article.)

ods, even near atomic resolution structures can be achieved (Schur et al., 2016).

Apart from averaging sub-volumes from a tomogram in order to increase resolution, one can look for known structures inside a tomogram. The structure of many molecular machines from cells are determined (e.g. from X-ray diffraction, cryoEM and NMR techniques) and available (e.g. from the Protein Data Bank (PDB); www.rcsb.org (Berman et al., 2000) or the Electron Microscopy Database (EMDB) (Lawson et al., 2016)). By utilizing a template-matching approach, an extensive six-dimensional (three spatial dimensions and three rotational dimensions) cross-correlational search between the molecular volume and the cellular tomogram can be performed to find the position and orientation of certain protein molecules inside parts of a cell (Nickell et al., 2006). Molecular crowding and low tomogram resolution limit the applicability of this technique (Beck et al., 2009), but huge improvements have been made using the state-of-the-art imaging techniques described herein (Mahamid et al., 2016).

4.4. Tomogram segmentation

As in medical tomographic reconstructions, the interpretation of 3D volume data is dependent on a specialist with a familiarity with the specimen and knowledge of the potential artifacts present in tomograms. Interpretation is difficult for the untrained eye because one is accustomed to looking at surfaces and not at noisy slices from volumes. Therefore, surface representation of the volumes into biologically-relevant segments greatly aids the interpretation and 3D view of the volume for both the trained and untrained eye (Fig. 10). A particular problem with (automated) segmentation of cryo-electron tomograms is that the volumes are noisy (due to the limited electron dose), anisotropically distorted (due to the tilt geometry/missing wedge), and that density values are not linear with the original signal (due to the CTF, phase contrast and reconstruction algorithms). In practice, structures of interest are often drawn by hand into the volume, which is both highly time-consuming and subjective. Automated segmentation is desirable because it is less user intensive and, more importantly, it provides an objective, reproducible way that allows interpretation and quantification of results. These objective, reproducible segmented tomograms can also be deposited in databases such as EMDB (Lawson et al., 2016). Identifying particular structures within cellular volumes is limited by the resolution of the tomogram. However, certain larger structures, such as actin filaments and microtubules, were successfully traced and segmented automatically by template matching of rod-like shapes (Rigort et al., 2012b; Rusu et al., 2012). Also, some initial attempts on segmentation of surfaces of liposomes were made (Koning et al., 2013). Even template matching of specific proteins inside cells is possible (Asano et al., 2015). The increasing quality of CET imaging and the resulting tomograms, combined with development and implementation of better and faster template matching, neural network algorithms and increasing computational resources makes it possible to automatically segment and/or template-match many of the larger structures inside cellular tomograms (Chen et al., 2017), and developments in related fields, such as multi-dimensional transfer function volume rendering (Kniss et al., 2002), are also expected to yield improvements in tomogram visualization.

5. Related techniques

Aside from the CET technique described above, which is based on 2D imaging at different angles, there are several related newly-developing cryo techniques that are worth mentioning in the context of three-dimensional imaging of cells and tissues in an anatomic setting: cryo serial block-face scanning electron microscopy (cryoSBF-SEM), which combines serial sectioning and imaging of surfaces with scanning electron microscopy (SEM), cryo soft X-ray tomography (cryoSXT), in which X-rays are used for imaging, and cryo correlative light and electron microscopy (cryoCLEM), which combines fluorescent light microscopy (fLM) imaging for targeting specific sites with CET.

5.1. CryoSBF-SEM

As well as generating 3D reconstructions by recombining angular views, volumes can also be generated by serial sectioning and subsequent imaging. In this technique, a block of tissue is cryo-fixed by HPF. One flat surface side of this tissue block is repeatedly imaged using SEM while consecutively slices are removed. Imaging and sectioning is repeated automatically hundreds of times so that effectively a 3D volume is constructed from the sample. The sectioning is performed inside the SEM either by a focused ion beam (FIB). 3D SEM results in relatively low-resolution images (with pixel sizes of a few nm in XY, whilst Z (height) is dependent on the thickness of the slice). The major advantage is that very large volumes can be imaged, which enormously extends the sample size range of typical tomographic EM imaging. This technique was mainly developed and applied for imaging plastic embedded and heavy metal stained brain tissue (Denk and Horstmann, 2004). Recently it was also applied on cryo-preserved zebrafish tail samples using cryoFIB-SEM (Vidavsky et al., 2016).

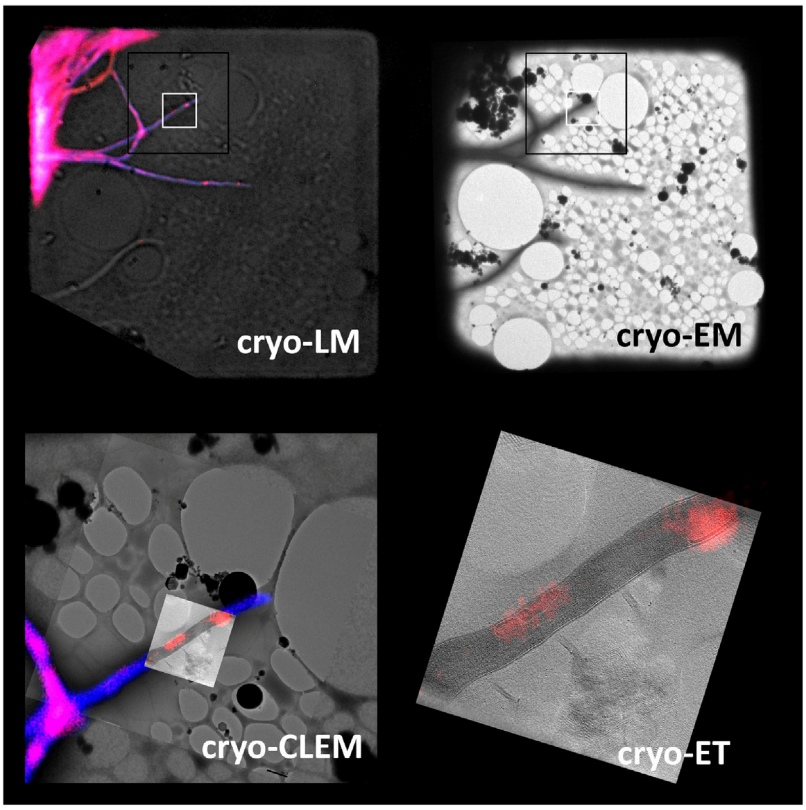

Fig. 11. Cryo-CLEM. Cryo correlative light and electron microscopy.
(A) Cryo-fluorescent light microscopy (cryo-fLM) imaging of fluorescently tagged Streptomyces bacterial cells can aid the targeting of certain structures. (B) Imaging cryoEM of the same area allows targeting of labeled structures in the electron microscope. (C) Higher magnification cryoEM imaging and accurate overlay determines the specific site for CET imaging. (D) Overlay of the cryo electron tomogram slice and the cryo-fLM lights up the labeled structures inside the cell.

5.2. CryoSXT

In cryo soft X-ray tomography (cryoSXT), like CET, a 3D volume of biological material is also reconstructed from a series of projection views, though with several differences. X-rays are used for imaging, and since they have larger penetration depth for vitrified biological samples than electrons, complete cells can be imaged. The soft X-rays have a tuned energy that falls within the so-called 'water window' (between 284–543 eV) which optimizes the absorption difference of X-rays between oxygen and carbon elements, which is the contrasting mechanism. The X-ray beam is focused onto the sample and the detector by zone-plates, X-ray diffracting elements. The current resolution is in the order of 25–35 nm. Correlative cryofLM/cryoSXT techniques are also developed and typical examples of cryo-SXT imaging are whole cell reconstructions of the yeast Saccharomyces cerevisiae. For a more in-depth review, see Carzaniga et al. (2014).

5.3. Cryo-correlative light and electron microscopy

The recent developments in CET enable imaging of macromolecular and protein structures inside cryogenically preserved cellular landscapes (Mahamid et al., 2016). Such high-resolution data sets rely on high-magnification tomograms, which limits the area that can be imaged. Specific positions or areas of interest can therefore be difficult to identify within the cell. One solution is to employ cryo-correlative light and electron microscopy (cryoCLEM), which combines CET with cryo-fLM of the same sample (Fig. 11). This is possible by using labelling techniques for fLM, either genetic tagging (such as GFP) or by chemical labeling using specific dyes to target and identify structures of interest, either in a two-step LM/EM approach (Celler et al., 2016; Hampton et al., 2017) or an integrated setup (Faas et al., 2013; Wang et al., 2017). Currently with cryo-CLEM, the resolution gap between fLM (~400 nm) and CET (~4 nm) is two orders of magnitude, although localization can be performed with a precision of ~40 nm with fLM (Schorb and Briggs, 2014). Nevertheless, targeting specific molecules inside a crowded landscape required higher cryo-fLM imaging techniques, such as super-resolution fLM (Wolff et al., 2016) for accurate localization, and future developments are targeted towards integrating these into cryo-CLEM. This will need adaptation of LM systems and the development of probes specifically for super-resolution cryoCLEM, but will allow multidimensional functional imaging of cellular landscapes at nanoscale resolution.

6. Conclusions and perspectives

Technical development and implementation in the last decade of designated cryo-electron microscopes, phase plate technology and direct electron detectors have dramatically improved both the speed and quality of CET. The improved resolution and interpretability of cryo-electron tomograms has broadened the applicability of CET to biological specimens and the attainable details that can be observed. These advances in CET shifted the resolution range of structural investigation from cellular morphology to the macromolecular level, enabling investigation into the underlying structural basis of immunity and infection, such as pleomorphic viruses such as HIV (Schur et al., 2016), membrane bound IgG-C1 immune complexes (Diebolder et al., 2014), complement membrane attack complex pores (Sharp et al., 2016), and the structure of Heliobacter pylori infectious systems (Ghosal et al., 2017).

Despite these recent advances, CET is still relatively labor-intensive and slow compared to SPA cryo-EM. Data collection of cryo-EM is largely automated, after setting imaging parameters and semi-automated targeting of imaging positions on the holey support. CET should be made faster by (i) automated targeting using CLEM by the integration with fluorescent light or raman microscopy techniques, and (ii) faster tilt series acquisition, which now typically takes approximately an hour, by implementation of more stable stage tilt behavior, adapted acquisition software and faster cameras, in order to allow a speed increase of circa a factor of 100 (Migunov et al., 2015). Furthermore, tomographic image reconstruction should be fully automated and integrated with acquisition and also robust in order to prevent large data storage requirements of intermediate raw files. Automatic segmentation, quantification and visualization by 3D surface rendering should be developed to aid interpretation of data. In order to make CET more widely applicable, designated CET microscope systems, comparable to medical imaging devices (CAT, MRI, CT) might be the way forward.

Due to the advances we have described, the ability to perform molecular imaging of subcellular structures at nanoscale level in vivo and in situ means that the applicability of CET to biology and medicine has never been higher. Future developments will only increase the relevancy of this technique to diagnostics. We will use these techniques to image biological processes in their native environment, such as cellular, viral and bacterial infections and immune complexes binding to cells, to elucidate the molecular mechanisms of disease.

Acknowledgements

This work has been supported by iNEXT, project number 653706, funded by the European Union's Horizon 2020 research and innovation programme under grant agreement 759517, the Dutch foundation STW Projects 13711, Nanosurf AG and SmartTip B.V., and 12713, Microscopy Valley, the Council for Chemical Sciences (CW) of the Netherlands Organization for Scientific Research (NWO grant 700.57.010). The authors acknowledge the support and the use of resources of Instruct, a Landmark ESFRI project. We thank Rob Hoeben, Ton Rabelink, Ton Raap and Peter Nibbering (LUMC) for critical reading of the manuscript.

References

Al-Amoudi, A., Chang, J.J., Leforestier, A., McDowall, A., Salamin, L.M., Norlen, L.P., Richter, K., Blanc, N.S., Studer, D., Dubochet, J., 2004a. Cryo-electron microscopy of vitreous sections. EMBO J. 23, 3583–3588.

Al-Amoudi, A., Norlen, L.P., Dubochet, J., 2004b. Cryo-electron microscopy of vitreous sections of native biological cells and tissues. J. Struct. Biol. 148, 131–135.

Amat, F., Castano-Diez, D., Lawrence, A., Moussavi, F., Winkler, H., Horowitz, M., 2010. Alignment of cryo-electron tomography datasets. Methods Enzymol. 482, 343–367.

Asano, S., Fukuda, Y., Beck, F., Aufderheide, A., Forster, F., Danev, R., Baumeister, W., 2015. Proteasomes. A molecular census of 26S proteasomes in intact neurons. Science 347, 439–442.

Baker, L.A., Rubinstein, J.L., 2010. Radiation damage in electron cryomicroscopy. Methods Enzymol. 481, 371–388.

Bauerlein, F.J.B., Saha, I., Mishra, A., Kalemanov, M., Martinez-Sanchez, A., Klein, R., Dudanova, I., Hipp, M.S., Hartl, F.U., Baumeister, W., Fernandez-Busnadiego, R., 2017. In situ architecture and cellular interactions of PolyQ inclusions. Cell 171, 179–187, e110.

Beck, M., Malmstrom, J.A., Lange, V., Schmidt, A., Deutsch, E.W., Aebersold, R., 2009. Visual proteomics of the human pathogen Leptospira interrogans. Nat. Methods 6, 817–823.

Berman, H.M., Westbrook, J., Feng, Z., Gilliland, G., Bhat, T.N., Weissig, H., Shindyalov, I.N., Bourne, P.E., 2000. The protein data bank. Nucleic Acids Res. 28, 235–242.

Bernstein, F.C., Koetzle, T.F., Williams, G.J., Meyer Jr., E.F., Brice, M.D., Rodgers, J.R., Kennard, O., Shimanouchi, T., Tasumi, M., 1977. The protein data bank: a computer-based archival file for macromolecular structures. J. Mol. Biol. 112, 535–542.

Carzaniga, R., Domart, M.C., Collinson, L.M., Duke, E., 2014. Cryo-soft X-ray tomography: a journey into the world of the native-state cell. Protoplasma 251, 449–458.

Castano-Diez, D., Scheffer, M., Al-Amoudi, A., Frangakis, A.S., 2010. Alignator: a GPU powered software package for robust fiducial-less alignment of cryo tilt-series. J. Struct. Biol. 170, 117–126.

Celler, K., Koning, R.I., Willemse, J., Koster, A.J., van Wezel, G.P., 2016. Cross-membranes orchestrate compartmentalization and morphogenesis in Streptomyces. Nat. Commun. 7, ncomms11836.

Chen, M., Dai, W., Sun, S.Y., Jonasch, D., He, C.Y., Schmid, M.F., Chiu, W., Ludtke, S.J., 2017. Convolutional neural networks for automated annotation of cellular cryo-electron tomograms. Nat. Methods 14, 983–985.

Dahl, R., Staehelin, L.A., 1989. High-pressure freezing for the preservation of biological structure: theory and practice. J. Electron Microsc. Tech. 13, 165–174.

Dai, W., Fu, C., Raytcheva, D., Flanagan, J., Khant, H.A., Liu, X., Rochat, R.H., Haase-Pettingell, C., Piret, J., Ludtke, S.J., Nagayama, K., Schmid, M.F., King, J.A., Chiu, W., 2013. Visualizing virus assembly intermediates inside marine cyanobacteria. Nature 502, 707–710.

Danev, R., Buijsse, B., Khoshouei, M., Plitzko, J.M., Baumeister, W., 2014. Volta potential phase plate for in-focus phase contrast transmission electron microscopy. Proc. Natl. Acad. Sci. U. S. A. 111, 15635–15640.

Danev, R., Glaeser, R.M., Nagayama, K., 2009. Practical factors affecting the performance of a thin-film phase plate for transmission electron microscopy. Ultramicroscopy 109, 312–325.

Danev, R., Nagayama, K., 2001. Transmission electron microscopy with Zernike phase plate. Ultramicroscopy 88, 243–252.

Denk, W., Horstmann, H., 2004. Serial block-face scanning electron microscopy to reconstruct three-dimensional tissue nanostructure. PLoS Biol. 2, e329.

Diebolder, C.A., Beurskens, F.J., de Jong, R.N., Koning, R.I., Strumane, K., Lindorfer, M.A., Voorhorst, M., Ugurlar, D., Rosati, S., Heck, A.J., van de Winkel, J.G., Wilson, I.A., Koster, A.J., Taylor, R.P., Saphire, E.O., Burton, D.R., Schuurman, J., Gros, P., Parren, P.W., 2014. Complement is activated by IgG hexamers assembled at the cell surface. Science 343, 1260–1263.

Diebolder, C.A., Faas, F.G., Koster, A.J., Koning, R.I., 2015. Conical Fourier shell correlation applied to electron tomograms. J. Struct. Biol. 190, 215–223.

Dierksen, K., Typke, D., Hegerl, R., Walz, J., Sackmann, E., Baumeister, W., 1995. Three-dimensional structure of lipid vesicles embedded in vitreous ice and investigated by automated electron tomography. Biophys. J. 68, 1416–1422.

Ding, H.J., Oikonomou, C.M., Jensen, G.J., 2015. The caltech tomography database and automatic processing pipeline. J. Struct. Biol. 192, 279–286.

Dubochet, J., Adrian, M., Chang, J.J., Homo, J.C., Lepault, J., McDowall, A.W., Schultz, P., 1988. Cryo-electron microscopy of vitrified specimens. Q. Rev. Biophys. 21, 129–228.

Egerton, R.F., 2011. Electron Energy-Loss Spectrosopy in the Electron Microscope. Springer.

Faas, F.G., Barcena, M., Agronskaia, A.V., Gerritsen, H.C., Moscicka, K.B., Diebolder, C.A., van Driel, L.F., Limpens, R.W., Bos, E., Ravelli, R.B., Koning, R.I., Koster, A.J., 2013. Localization of fluorescently labeled structures in frozen-hydrated samples using integrated light electron microscopy. J. Struct. Biol. 181, 283–290.

Feja, B., Aebi, U., 1999. Determination of the inelastic mean free path of electrons in vitrified ice layers for on-line thickness measurements by zero-loss imaging. J. Microsc. 193, 15–19.

Fernandez, J.J., Li, S., Crowther, R.A., 2006. CTF determination and correction in electron cryotomography. Ultramicroscopy 106, 587–596.

Fernandez-Leiro, R., Scheres, S.H., 2016. Unravelling biological macromolecules with cryo-electron microscopy. Nature 537, 339–346.

Fukuda, Y., Laugks, U., Lucic, V., Baumeister, W., Danev, R., 2015. Electron cryotomography of vitrified cells with a Volta phase plate. J. Struct. Biol. 190, 143–154.

Ghosal, D., Chang, Y.W., Jeong, K.C., Vogel, J.P., Jensen, G.J., 2017. In situ structure of the Legionella Dot/Icm type IV secretion system by electron cryotomography. EMBO Rep. 18, 726–732.

Gilbert, P., 1972. Iterative methods for the three-dimensional reconstruction of an object from projections. J. Theor. Biol. 36, 105–117.

Glaeser, R.M., 1971. Limitations to significant information in biological electron microscopy as a result of radiation damage. J. Ultrastruct. Res. 36, 466–482.

Grange, M., Vasishtan, D., Grunewald, K., 2017. Cellular electron cryo tomography and in situ sub-volume averaging reveal the context of microtubule-based processes. J. Struct. Biol. 197, 181–190.

Grimm, R., Typke, D., Barmann, M., Baumeister, W., 1996. Determination of the inelastic mean free path in ice by examination of tilted vesicles and automated most probable loss imaging. Ultramicroscopy 63, 169–179.

Guckenberger, R., 1982. Determination of a common origin in the micrographs of tilt series in three-dimensional electron microscopy. Ultramicroscopy 9, 167–173.

Haider, M., Hartel, P., Muller, H., Uhlemann, S., Zach, J., 2009. Current and future aberration correctors for the improvement of resolution in electron microscopy. Philos. Trans. A Math. Phys. Eng. Sci. 367, 3665–3682.

Hampton, C.M., Strauss, J.D., Ke, Z., Dillard, R.S., Hammonds, J.E., Alonas, E., Desai, T.M., Marin, M., Storms, R.E., Leon, F., Melikyan, G.B., Santangelo, P.J., Spearman, P.W., Wright, E.R., 2017. Correlated fluorescence microscopy and cryo-electron tomography of virus-infected or transfected mammalian cells. Nat. Protoc. 12, 150–167.

Han, H.M., Huebinger, J., Grabenbauer, M., 2012. Self-pressurized rapid freezing (SPRF) as a simple fixation method for cryo-electron microscopy of vitreous sections. J. Struct. Biol. 178, 84–87.

Han, K.F., Sedat, J.W., Agard, D.A., 1995. Mechanism of image formation for thick biological specimens: exit wavefront reconstruction and electron energy-loss spectroscopic imaging. J. Microsc. 178, 107–119.

Han, R., Wang, L., Liu, Z., Sun, F., Zhang, F., 2015. A novel fully automatic scheme for fiducial marker-based alignment in electron tomography. J. Struct. Biol. 192, 403–417.
Hayles, M.F., de Winter, D.A., Schneijdenberg, C.T., Meeldijk, J.D., Luecken, U., Persoon, H., de Water, J., de Jong, F., Humbel, B.M., Verkleij, A.J., 2010. The making of frozen-hydrated, vitreous lamellas from cells for cryo-electron microscopy. J. Struct. Biol. 172, 180–190.
Henderson, R., 1995. The potential and limitations of neutrons, electrons and X-rays for atomic resolution microscopy of unstained biological molecules. Q. Rev. Biophys. 28, 171–193.
Iudin, A., Korir, P.K., Salavert-Torres, J., Kleywegt, G.J., Patwardhan, A., 2016. EMPIAR: a public archive for raw electron microscopy image data. Nat. Methods 13, 387–388.
Kniss, J., Kindlmann, G., Hansen, C., 2002. Multi-dimensional transfer functions for interactive volume rendering. IEEE Trans. Vis. Comput. Graph. 8 (3), 270–285.
Koning, R.I., de Breij, A., Oostergetel, G.T., Nibbering, P.H., Koster, A.J., Dijkshoorn, L., 2013. Cryo-electron tomography analysis of membrane vesicles from *Acinetobacter baumannii* ATCC19606T. Res. Microbiol. 164, 397–405.
Koning, R.I., Koster, A.J., 2009. Cryo-electron tomography in biology and medicine. Ann. Anat. 191, 427–445.
Koster, A.J., Chen, H., Sedat, J.W., Agard, D.A., 1992. Automated microscopy for electron tomography. Ultramicroscopy 46, 207–227.
Koster, A.J., Grimm, R., Typke, D., Hegerl, R., Stoschek, A., Walz, J., Baumeister, W., 1997. Perspectives of molecular and cellular electron tomography. J. Struct. Biol. 120, 276–308.
Krivanek, O.L., Friedman, S.L., Gubbens, A.J., Kraus, B., 1995. An imaging filter for biological applications. Ultramicroscopy 59, 267–282.
Krivanek, O.L., Mooney, P.E., 1993. Applications of slow-scan CCD cameras in transmission electron microscopy. Ultramicroscopy 49.
Krueger, R., 1999. Dual-column (FIB–SEM) wafer applications. Micron 30, 221–226.
Kuhlbrandt, W., 2014. Biochemistry. The resolution revolution. Science 343, 1443–1444.
Lanio, S., Rose, H., Krahl, D., 1986. Test and improved design of a corrected imaging magnetic energy filter. Optik 73, 56–63.
Lawson, C.L., Patwardhan, A., Baker, M.L., Hryc, C., Garcia, E.S., Hudson, B.P., Lagerstedt, I., Ludtke, S.J., Pintilie, G., Sala, R., Westbrook, J.D., Berman, H.M., Kleywegt, G.J., Chiu, W., 2016. EMDataBank unified data resource for 3DEM. Nucleic Acids Res. 44, D396–D403.
Leunissen, J.L., Yi, H., 2009. Self-pressurized rapid freezing (SPRF): a novel cryofixation method for specimen preparation in electron microscopy. J. Microsc. 235, 25–35.
Luther, P.K., Lawrence, M.C., Crowther, R.A., 1988. A method for monitoring the collapse of plastic sections as a function of electron dose. Ultramicroscopy 24, 7–18.
Mahamid, J., Pfeffer, S., Schaffer, M., Villa, E., Danev, R., Cuellar, L.K., Forster, F., Hyman, A.A., Plitzko, J.M., Baumeister, W., 2016. Visualizing the molecular sociology at the HeLa cell nuclear periphery. Science 351, 969–972.
Malac, M., Beleggia, M., Kawasaki, M., Li, P., Egerton, R.F., 2012. Convenient contrast enhancement by a hole-free phase plate. Ultramicroscopy 118, 77–89.
Marabini, R., Carragher, B., Chen, S., Chen, J., Cheng, A., Downing, K.H., Frank, J., Grassucci, R.A., Bernard Heymann, J., Jiang, W., Jonic, S., Liao, H.Y., Ludtke, S.J., Patwari, S., Piotrowski, A.L., Quintana, A., Sorzano, C.O., Stahlberg, H., Vargas, J., Voss, N.R., Chiu, W., Carazo, J.M., 2015. CTF challenge: result summary. J. Struct. Biol. 190, 348–359.
Marko, M., Hsieh, C., Schalek, R., Frank, J., Mannella, C., 2007. Focused-ion-beam thinning of frozen-hydrated biological specimens for cryo-electron microscopy. Nat. Methods 4, 215–217.
Mastronarde, D.N., 1997. Dual-axis tomography: an approach with alignment methods that preserve resolution. J. Struct. Biol. 120, 343–352.
Mastronarde, D.N., 2005. Automated electron microscope tomography using robust prediction of specimen movements. J. Struct. Biol. 152, 36–51.
Mastronarde, D.N., Held, S.R., 2017. Automated tilt series alignment and tomographic reconstruction in IMOD. J. Struct. Biol. 197, 102–113.
McDonald, K.L., Auer, M., 2006. High-pressure freezing, cellular tomography, and structural cell biology. Biotechniques 41, 137, 139, 141 passim.
McMullan, G., Faruqi, A.R., Clare, D., Henderson, R., 2014. Comparison of optimal performance at 300 keV of three direct electron detectors for use in low dose electron microscopy. Ultramicroscopy 147, 156–163.
Merk, A., Bartesaghi, A., Banerjee, S., Falconieri, V., Rao, P., Davis, M.I., Pragani, R., Boxer, M.B., Earl, L.A., Milne, J.L., Subramaniam, S., 2016. Breaking cryo-EM resolution barriers to facilitate drug discovery. Cell 165, 1698–1707.
Migunov, V., Ryll, H., Zhuge, X., Simson, M., Struder, L., Batenburg, K.J., Houben, L., Dunin-Borkowski, R.E., 2015. Rapid low dose electron tomography using a direct electron detection camera. Sci. Rep. 5, 14516.
Moor, H., Riehle, U., 1968. Snap-freezing under high pressure: a new fixation technique for freeze-etching. Proc. Fourth Europ. Reg. Conf. Elect. Microsc. 2.
Nickell, S., Forster, F., Linaroudis, A., Net, W.D., Beck, F., Hegerl, R., Baumeister, W., Plitzko, J.M., 2005. TOM software toolbox: acquisition and analysis for electron tomography. J. Struct. Biol. 149, 227–234.
Nickell, S., Kofler, C., Leis, A.P., Baumeister, W., 2006. A visual approach to proteomics. Nat. Rev. Mol. Cell Biol. 7, 225–230.
Noble, A.J., Stagg, S.M., 2015. Automated batch fiducial-less tilt-series alignment in Appion using Protomo. J. Struct. Biol. 192, 270–278.
Palmer, C.M., Lowe, J., 2014. A cylindrical specimen holder for electron cryotomography. Ultramicroscopy 137, 20–29.
Patwardhan, A., Ashton, A., Brandt, R., Butcher, S., Carzaniga, R., Chiu, W., Collinson, L., Doux, P., Duke, E., Ellisman, M.H., Franken, E., Grunewald, K., Heriche, J.K., Koster, A., Kuhlbrandt, W., Lagerstedt, I., Larabell, C., Lawson, C.L., Saibil, H.R., Sanz-Garcia, E., Subramaniam, S., Verkade, P., Swedlow, J.R., Kleywegt, G.J., 2014. A 3D cellular context for the macromolecular world. Nat. Struct. Mol. Biol. 21, 841–845.
Patwardhan, A., Brandt, R., Butcher, S.J., Collinson, L., Gault, D., Grunewald, K., Hecksel, C., Huiskonen, J.T., Iudin, A., Jones, M.L., Korir, P.K., Koster, A.J., Lagerstedt, I., Lawson, C.L., Mastronarde, D., McCormick, M., Parkinson, H., Rosenthal, P.B., Saalfeld, S., Saibil, H.R., Sarntivijai, S., Solanes Valero, I., Subramaniam, S., Swedlow, J.R., Tudose, I., Winn, M., Kleywegt, G.J., 2017. Building bridges between cellular and molecular structural biology. Elife 6.
Penczek, P., Marko, M., Buttle, K., Frank, J., 1995. Double-tilt electron tomography. Ultramicroscopy 60, 393–410.
Pfeffer, S., Brandt, F., Hrabe, T., Lang, S., Eibauer, M., Zimmermann, R., Forster, F., 2012. Structure and 3D arrangement of endoplasmic reticulum membrane-associated ribosomes. Structure 20, 1508–1518.
Radermacher, M., 1988. Three-dimensional reconstruction of single particles from random and nonrandom tilt series. J. Electron Microsc. Tech. 9, 359–394.
Richter, K., 1994. Cutting artefacts on ultrathin cryosections of biological bulk specimens. Micron 25, 297–308.
Rigort, A., Bauerlein, F.J., Villa, E., Eibauer, M., Laugks, T., Baumeister, W., Plitzko, J.M., 2012a. Focused ion beam micromachining of eukaryotic cells for cryoelectron tomography. Proc. Natl. Acad. Sci. U. S. A. 109, 4449–4454.
Rigort, A., Gunther, D., Hegerl, R., Baum, D., Weber, B., Prohaska, S., Medalia, O., Baumeister, W., Hege, H.C., 2012b. Automated segmentation of electron tomograms for a quantitative description of actin filament networks. J. Struct. Biol. 177, 135–144.
Rigort, A., Plitzko, J.M., 2015. Cryo-focused-ion-beam applications in structural biology. Arch. Biochem. Biophys. 581, 122–130.
Rusu, M., Starosolski, Z., Wahle, M., Rigort, A., Wriggers, W., 2012. Automated tracing of filaments in 3D electron tomography reconstructions using Sculptor and Situs. J. Struct. Biol. 178, 121–128.
Schorb, M., Briggs, J.A., 2014. Correlated cryo-fluorescence and cryo-electron microscopy with high spatial precision and improved sensitivity. Ultramicroscopy 143, 24–32.
Schur, F.K., Obr, M., Hagen, W.J., Wan, W., Jakobi, A.J., Kirkpatrick, J.M., Sachse, C., Krausslich, H.G., Briggs, J.A., 2016. An atomic model of HIV-1 capsid-SP1 reveals structures regulating assembly and maturation. Science 353, 506–508.
Sharp, T.H., Faas, F.G., Koster, A.J., Gros, P., 2017. Imaging complement by phase-plate cryo-electron tomography from initiation to pore formation. J. Struct. Biol. 197 (2), 155–162.
Sharp, T.H., Koster, A.J., Gros, P., 2016. Heterogeneous MAC initiator and pore structures in a lipid bilayer by phase-plate cryo-electron tomography. Cell Rep. 15, 1–8.
Sorzano, C.O., Messaoudi, C., Eibauer, M., Bilbao-Castro, J.R., Hegerl, R., Nickell, S., Marco, S., Carazo, J.M., 2009. Marker-free image registration of electron tomography tilt-series. BMC Bioinform. 10, 124.
Spence, J.C.H., Zuo, J.M., 1988. A large dynamic range parallel detection CCD system for electron diffraction and imaging. J. Sci. Instrum. 59.
Studer, D., Graber, W., Al-Amoudi, A., Eggli, P., 2001. A new approach for cryofixation by high-pressure freezing. J. Microsc. 203, 285–294.
Studer, D., Humbel, B.M., Chiquet, M., 2008. Electron microscopy of high pressure frozen samples: bridging the gap between cellular ultrastructure and atomic resolution. Histochem. Cell Biol. 130, 877–889.
Tanaka, M., Tsuda, K., Terauchi, M., Tsuno, K., Kaneyama, T., Honda, T., Ishida, M., 1999. A new 200 kV omega-filter electron microscope. J. Microsc. 194, 219–227.
Turonova, B., Schur, F.K.M., Wan, W., Briggs, J.A.G., 2017. Efficient 3D-CTF correction for cryo-electron tomography using NovaCTF improves subtomogram averaging resolution to 3.4 A. J. Struct. Biol. 199 (3), 187–195.
Unverdorben, P., Beck, F., Sledz, P., Schweitzer, A., Pfeifer, G., Plitzko, J.M., Baumeister, W., Forster, F., 2014. Deep classification of a large cryo-EM dataset defines the conformational landscape of the 26S proteasome. Proc. Natl. Acad. Sci. U. S. A. 111, 5544–5549.
Vanhecke, D., Graber, W., Studer, D., 2008. Close-to-native ultrastructural preservation by high pressure freezing. Methods Cell Biol. 88, 151–164.
Verkade, P., 2008. Moving EM: the rapid transfer system as a new tool for correlative light and electron microscopy and high throughput for high-pressure freezing. J. Microsc. 230, 317–328.
Vidavsky, N., Akiva, A., Kaplan-Ashiri, I., Rechav, K., Addadi, L., Weiner, S., Schertel, A., 2016. Cryo-FIB-SEM serial milling and block face imaging: large volume structural analysis of biological tissues preserved close to their native state. J. Struct. Biol. 196, 487–495.
Walz, J., Typke, D., Nitsch, M., Koster, A.J., Hegerl, R., Baumeister, W., 1997. Electron tomography of single ice-embedded macromolecules: three-dimensional alignment and classification. J. Struct. Biol. 120, 387–395.
Wan, W., Kolesnikova, L., Clarke, M., Koehler, A., Noda, T., Becker, S., Briggs, J.A.G., 2017. Structure and assembly of the Ebola virus nucleocapsid. Nature 551, 394–397.
Wang, S., Li, S., Ji, G., Huang, X., Sun, F., 2017. Using integrated correlative cryo-light and electron microscopy to directly observe syntaphilin-immobilized neuronal mitochondria in situ. Biophys. Rep. 3, 8–16.
Winkler, H., Taylor, K.A., 2013. Marker-free dual-axis tilt series alignment. J. Struct. Biol. 182, 117–124.
Wolff, G., Hagen, C., Grunewald, K., Kaufmann, R., 2016. Towards correlative superresolution fluorescence and electron cryo-microscopy. Biol. Cell 108, 245–258.

Xiong, Q., Morphew, M.K., Schwartz, C.L., Hoenger, A.H., Mastronarde, D.N., 2009. CTF determination and correction for low dose tomographic tilt series. J. Struct. Biol. 168, 378–387.

Xuong, N.H., Jin, L., Kleinfelder, S., Li, S., Leblanc, P., Duttweiler, F., Bouwer, J.C., Peltier, S.T., Milazzo, A.C., Ellisman, M., 2007. Future directions for camera systems in electron microscopy. Methods Cell Biol. 79, 721–739.

Zheng, Q.S., Braunfeld, M.B., Sedat, J.W., Agard, D.A., 2004. An improved strategy for automated electron microscopic tomography. J. Struct. Biol. 147, 91–101.

Zheng, S.Q., Branlund, E., Kesthelyi, B., Braunfeld, M.B., Cheng, Y., Sedat, J.W., Agard, D.A., 2011. A distributed multi-GPU system for high speed electron microscopic tomographic reconstruction. Ultramicroscopy 111, 1137–1143.

Zheng, S.Q., Keszthelyi, B., Branlund, E., Lyle, J.M., Braunfeld, M.B., Sedat, J.W., Agard, D.A., 2007. UCSF tomography: an integrated software suite for real-time electron microscopic tomographic data collection, alignment, and reconstruction. J. Struct. Biol. 157, 138–147.

Ziese, U., Janssen, A.H., Murk, J.L., Geerts, W.J., Van der Krift, T., Verkleij, A.J., Koster, A.J., 2002. Automated high-throughput electron tomography by pre-calibration of image shifts. J. Microsc. 205, 187–200.